ACS SENSORS

pubs.acs.org/acssensors Article

Improving Real-Time In Vivo Molecular Monitoring: Multi-Gaussian with Laplacian Voltammogram Fitting Enhances the Precision of Electrochemical Aptamer-Based Sensors

Zeki Duman, Nicole A. Emmons, Tod E. Kippin, Lior Sepunaru, João Hespanha, and Kevin W. Plaxco*

Cite This: https://doi.org/10.1021/acssensors.5c00760 Read Online

ACCESS | Metrics & More | Article Recommendations | Supporting Information

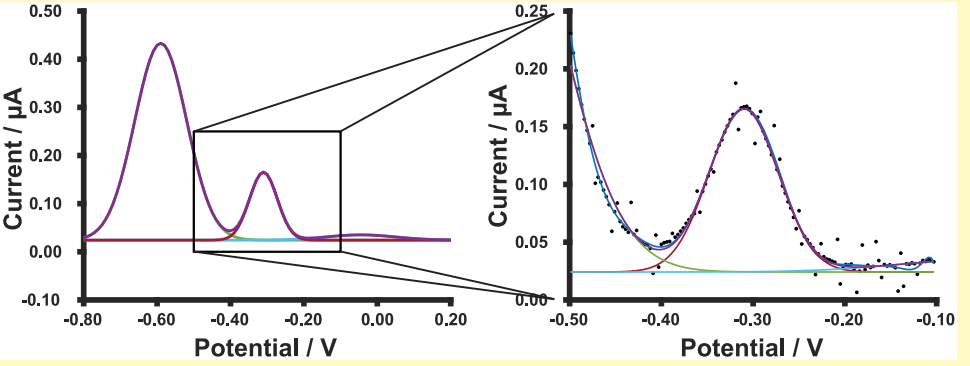

ABSTRACT: Electrochemical, aptamer-based (EAB) sensors are the first technology supporting high-frequency, real-time measurements of the concentrations of specific drugs, metabolites, and biomarkers in the body that is independent of the chemical reactivity of its analytes. To achieve this, EAB sensors employ the binding-induced folding of an electrode-attached, redox-reporter-modified aptamer to produce an electrochemical output easily monitored using square wave voltammetry. Using such sensors, multiple research groups have achieved the seconds-resolved, multihour measurement of multiple drugs and metabolites in situ in the veins, brains, and peripheral solid tissues of live animals. Historically, the large volume of voltammograms (hundreds per hour) produced by in vivo EAB sensors have been fitted using simple polynomials to extract the peak heights from which target concentrations are estimated. This, however, can lead to misestimation of peak heights due to overfitting of noise or poor correction of peak shouldering. In response, here we describe an alternative method of fitting EAB sensor voltammograms that improves the accuracy of "problematic" (i.e., noisy, or heavily "shouldered") data sets while simultaneously reducing sensor noise.

KEYWORDS: *biosensor, EABs, electrochemistry, fitting, software*

The ability to measure specific molecules in situ in the living body in real time and with seconds resolution could revolutionize both biomedical science and clinical practice. Such an ability would provide, for example, real-time information regarding organ function (e.g., the measurement of creatinine as a real-time measure of kidney function) and the high-resolution monitoring and delivery of therapy (e.g.,) therapeutic drug monitoring and closed-loop, feedback-controlled drug delivery.[1,2] To this end we (e.g.,[3−7]), and others (e.g.,[8−12]), are developing electrochemical aptamer-based (EAB) sensors, a sensing technology comprised of a redox-reporter-modified, target-recognizing aptamer attached to a gold electrode (Figure 1A). The binding of target to this aptamer induces a reversible conformational change that, in turn, alters the rate of electron transfer from the redox reporter (presumably due to changes in transport kinetics[13]) in a manner readily monitored using square wave voltammetry (Figure 1B). The rapidly reversible nature of the EAB signaling mechanism renders these sensors able to perform high-frequency measurements. And its high selectivity renders the approach adaptable to measurements in situ in the body (Figure 1C). Building on these advantages, EAB sensors have been used in the real-time monitoring of multiple drugs and metabolites in the plasma,[3−6] cerebrospinal fluid,[2,14] and interstitial fluid[8,9] of live rats. These successes suggest that EAB sensors may prove a powerful new approach to therapeutic drug monitoring, drug delivery, and the real-time measurement of biomarkers indicative of both illness and health.

The interrogation of high-time-resolution EAB sensors generates large (typically hundreds per hour) numbers of

Received: March 6, 2025
Revised: April 22, 2025
Accepted: May 13, 2025

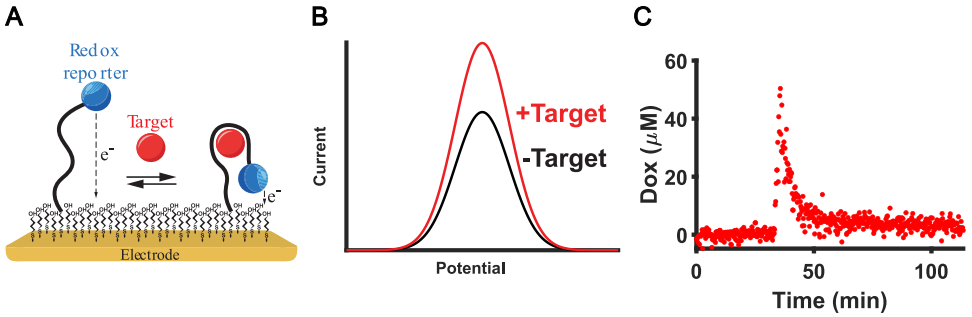

Figure 1. (A) Electrochemical, aptamer-based (EAB) sensors consist of a target-recognizing aptamer attached at one end to an electrode surface and modified at the other with a redox reporter. When the aptamer binds to its target, it undergoes a conformational change that alters the rate of electron transfer between the redox reporter and the electrode. (B) This change in electron transfer kinetics is easily monitored using square wave voltammetry. (C) From the monotonic relationship between aptamer occupancy and voltammetric peak current, we can determine the target's concentration (shown is the chemotherapeutic doxorubicin in situ in the rat jugular vein following an intravenous dosing of the drug at 35 min) in real time and with seconds resolution. Here we explore alternative methods of fitting the voltammograms to reduce noise in the concentration estimates produced by EAB sensors. Reproduced from.[21] Copyright 2025, American Chemical Society.

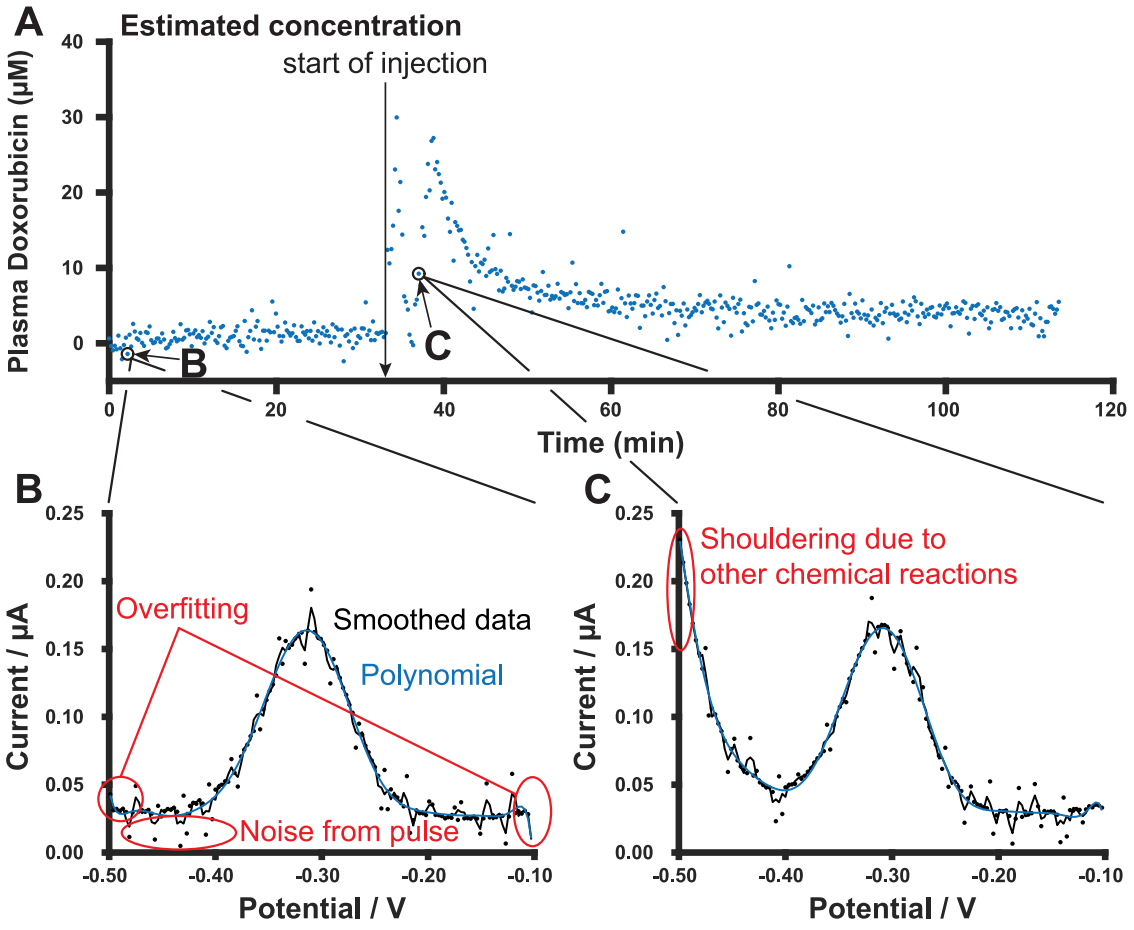

Figure 2. Polynomial fits do not always report accurately on the change in peak height produced by target binding, leading to error and noise in our estimations of target concentration. (A) The experimental data shown here are a set of estimated plasma doxorubicin concentrations collected before, during, and following an 8 mg/kg intravenous infusion. Based on both pharmacology and prior experience we expect such concentrations to rise monotonically during and shortly after the infusion, before then monotonically falling as the drug is eliminated from the plasma. The double-peaked profile seen, however, arises due to technical artifacts that we hope to solve using alternative voltammogram fitting approaches. (B) EAB sensor voltammograms, such as these, that are collected in the jugular exhibit significant noise, much of which arises due to the animal's pulse.[22] To estimate the voltammogram peak heights (from which we derive concentration estimates) in the presence of this noise, in our previous work we performed Savitzky-Golay smoothing, fit the smoothed values to a 15th order polynomial, and then took the difference between the maximum and minimum values of this fitted curve. Due to overfitting of residual noise at the edges of the potential window, however, this sometimes overestimates peak height. (C) Sensor degradation or, as seen here, the presence of high concentrations of a target that is electroactive, can cause shouldering. If the maximum value produced by the shoulder exceeds the height of the actual voltammogram peak, our naïve polynomial fitting will again misestimate peak height.

https://doi.org/10.1021/acssensors.5c00760
ACS Sens. XXXX, XXX, XXX−XXX

square wave voltammograms, which must then be fitted to determine the peak heights from which concentration estimates are derived. These voltammograms, however, are inevitably "degraded" by a variety of sources of both noise (as discussed below, both white and otherwise) and systematic distortions (e.g., shouldering from other faradaic processes), reducing the accuracy and precision of EAB sensor measurements. Specifically, the voltammograms produced by in vivo EAB sensors suffer from a variety of both random and systematic errors. Previously, we, and others (e.g.,[15−17]), have surmounted these issues by smoothing the voltammograms (using Savitzky−Golay filtering[18]), fitting them to a 15th order polynomial (which was chosen empirically as being sufficient to capture key details in the voltammograms), and then extracting the maximum and the minimum value of this curve to estimate the height of the voltammetric peak.[20] This approach, however, suffers from several potentially important limitations (described below) that reduce the accuracy and precision of the resulting in vivo concentration estimates.[19] Other strategies to analyze square wave voltammograms include machine learning algorithms[33,34] and to focus on the additional regions of potential scan where non-faradaic currents dominate.[35] The former, however, requires machine learning expertise which, in turn, requires tailoring for each specific set of experimental conditions, and the latter relies on specialized effort to identify a region of the voltammogram in which non-faradaic currents are not contributing significantly. Here, in contrast, we have developed methods of voltammogram fitting that are as general as the polynomial approach and yet reduce its potential sources of error. The resulting algorithm, which can be employed using standard square wave voltammetry data by any laboratory, significantly improves EAB-sensor-derived, in vivo concentration estimates.

RESULTS AND DISCUSSION

As our initial, "test-bed" data set we employed plasma doxorubicin measurements collected in the jugular vein of a live rat (Figure 2A). Specifically, we employed a data set that is particularly problematic, in part because the sensor was placed in quite close to the heart (producing significant noise due to the animal's pulse[22]), and in part because the target, doxorubicin, is itself electroactive,[23] causing a spurious signal at the highest target concentrations. Specifically, the latter produces significant "shouldering" at high plasma drug concentrations, as the direct oxidation of the target molecule produces a faradaic peak that is so large its shoulder intrudes into the potential window under observation. Then, after exploring this particularly difficult, noise-and-bias-filled example, we apply our new approach to in vivo data sets collected in other bodily compartments or in the measurement of other drugs.

The polynomial fits we have historically employed to estimate the peak heights of EAB sensor voltammograms fail to properly fit our voltammograms for at least three reasons. First, they are prone to overfitting, particularly in jugular placements for which there is significant noise associated with the animal's pulse. Specifically, the polynomial fit, which employs a 15th order polynomial including 16 estimated parameters, tends to overfit around the boundary points of the scanned voltage range, resulting in fits that trend strongly upward or downward at the edges of the potential window if noise is present (Figure 2B). And while the former does not affect the estimated peak height, the latter produces an artifactually low point on the curve, causing this fitting approach to overestimate the true peak height. Second, the polynomial fit fails in the presence of significant shouldering, which, while it occurs in our test-bed data set due to the presence of the redox-active analyte doxorubicin, can also occur when other faradic reactions occurring at potentials far from that of the redox reporter nevertheless contribute to the current observed in the potential window, such as the reduction of oxygen when the monolayer has become compromised. When this shouldering becomes large, the naive polynomial fit misassigns the shoulder as peak, thus causing it to overestimate peak height (Figure 2C). Finally, even minor shouldering contributes to the baseline current, causing the polynomial fit to underestimate the true peak height. While the latter two problems are particularly acute in our (notably poor quality) test bed data set, causing the estimated plasma drug concentration to rise, fall, and then rise again immediately after drug injection (Figure 2A), (behavior that is physiologically implausible), it is seen to a greater or lesser extent in many in vivo data sets (see below).

A complete theoretical description of a quasi-reversible square wave voltammogram[24] is nearly as complex as the 15th order polynomials employed in earlier work. Given this, as our first step we explored modeling the voltammogram peak as a simpler, bell-shaped curve. Specifically, fitting the true theoretical curve shape, which is too complex to fit to our data in real-time, to either a Gaussian or a Lorentzian curve shape, we find that the former better approximates the expected theoretical shape of a quasi-reversible square-wave voltammetric peak (Figure 3).

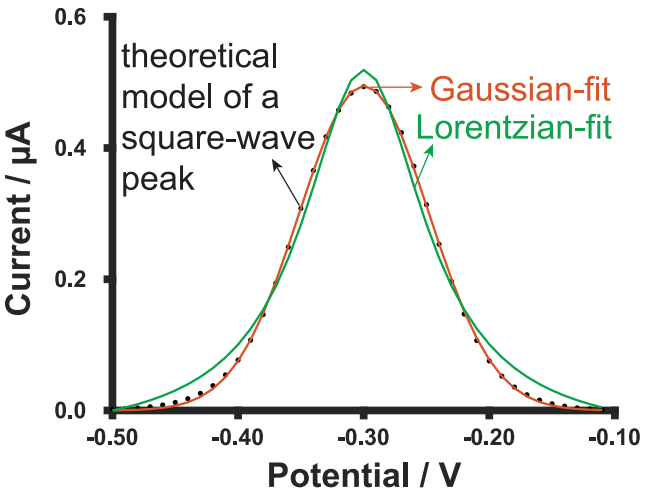

Figure 3. Gaussian curve (red) closely approximates the theoretical line shape (points) expected for an ideal square voltammogram peak arising from a surface-bound redox moiety.[24] A Lorentzian curve (green), in contrast, approximates the expected line shape rather more poorly.

Indeed, at any reasonable scale, a Gaussian curve appears indistinguishable from the complete theoretical description of such a peak. And, critically, it can be fitted to voltammogram data rapidly enough to support real-time measurements. We note, too, that, in addition to the Gaussian and Lorentzian functions, we also explored the hyperbolic secant and the square of hyperbolic secant functions. We find that the former, however, is not as accurate an approximation of square wave voltammograms as the Gaussian. And while the fit of the latter was similar to (though not improved results) that of the Gaussian, it is far slower computationally and thus we did not explore it further.

https://doi.org/10.1021/acssensors.5c00760
ACS Sens. XXXX, XXX, XXX−XXX

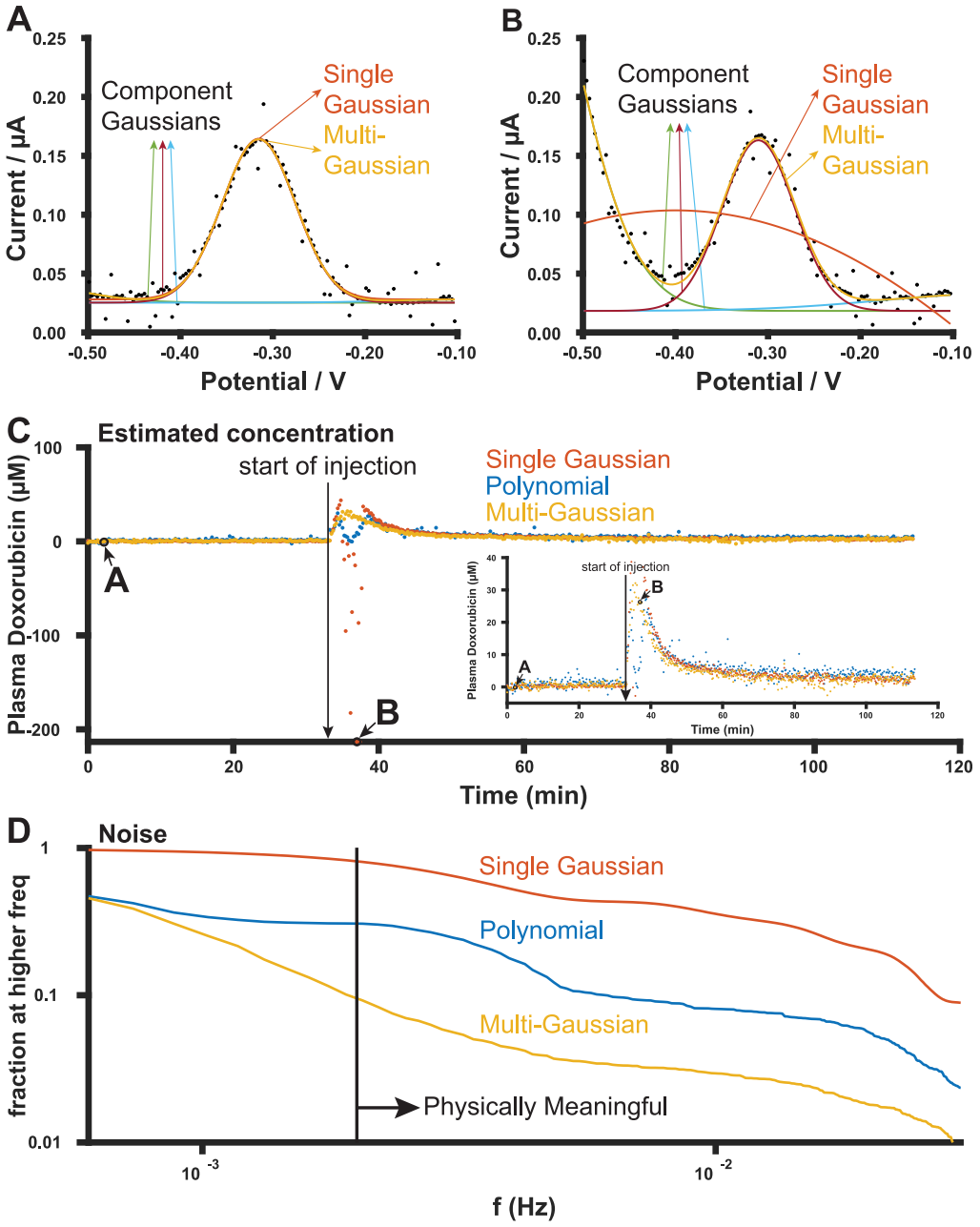

Figure 4. Here we compare the prior, polynomial fitting approach with single- and multi-Gaussian fits. (A) Fitting EAB-sensor voltammograms to a single Gaussian, which is described by just 4 fitted parameters, reduces the problem of overfitting at the extrema seen with our earlier, polynomial fitting approach, which described the curve using 16 fitted parameters. For a noisy, but "shoulder-free" voltammogram the multi-Gaussian fit is almost indistinguishable from the single-Gaussian fit. Likewise, the multi-Gaussian fit describes the peak shape of this relatively less challenging voltammogram quite well. This fit describes the peak as the sum of 3 Gaussians, one with its center below the low end of the potential window, a second with its center above the high-end of the potential window, and a third that represents the EAB sensor peak itself. (B) Like the polynomial fit, however, the single-Gaussian fit fails when faced with significant "shouldering." That is, when faradaic processes peaking outside of the observed potential window become so large that their shoulder begins to contribute significantly to the current seen in the potential window. In contrast, the multi-Gaussian fit successfully captures and corrects this effect. (C) For our test-bed intravenous data set, this shouldering leads to significant errors in the estimated drug concentration when we employ the polynomial or single-Gaussian fits. The latter is seen in the physically meaningless, negative concentrations estimated around what should, in fact, be the maximum plasma drug concentration. The multi-Gaussian fit, in contrast, alleviates both the nonphysiological double peak estimated by the polynomial fit and the physically impossible negative concentration estimates returned by the single-Gaussian fit. (D) The multi-Gaussian fit also reduces noise. This can be seen by observing that the fraction of the total variance (depicted on the *y*-axis) above a given frequency, f = 2 mHz (which corresponds to a time scale of 8 min, beyond which physiology-driven variations in drug concentration dominate the signal change), and above (depicted on the *x*-axis) is lower for the multi-Gaussian fit, which indicates a lower level of noise as physiology-driven processes are unlikely to explain variations in the estimated concentration at these fast time scales.

The single-Gaussian fit, which includes only 4 estimated parameters (the baseline current, the peak current, and mean potential and standard deviation of the Gaussian), effectively ignores the relatively small number of outlier points, making it less sensitive to noise at the edges of the potential window. This, in turn, renders its estimation of the voltammetric baseline more f4

https://doi.org/10.1021/acssensors.5c00760
ACS Sens. XXXX, XXX, XXX−XXX

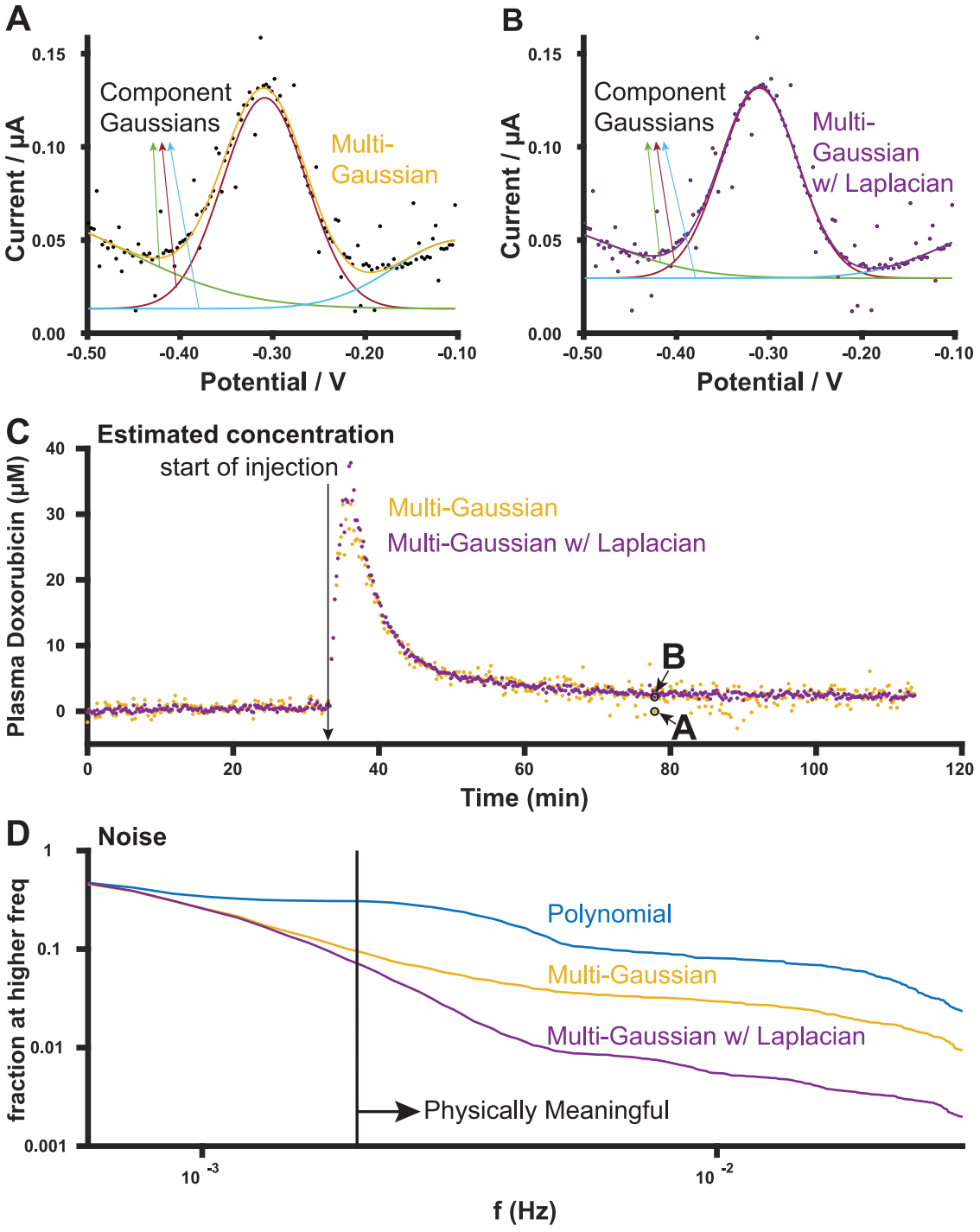

Figure 5. (A) While performing better than the single-Gaussian fit, the multi-Gaussian fit still sometimes converges to incorrect baseline value due to the large, regular noise associated with the animal's pulse. (B) To reduce this source of error, we next implemented L1 norm regularization. In this, we add a Laplacian term to the multi-Gaussian, which improves our ability to capture the outlier points in the voltammogram. (C) As expected, this does not significantly alter mean concentration estimates, but (D) it does significantly reduce noise relative to the other voltammogram fitting methods we have employed.

f4

accurate (Figure 4A). But because Gaussian fits fail to account for shouldering, it can produce highly inaccurate estimations of the peak height (Figure 4B). Inaccurate enough that, for our test bed data set, the Gaussian fit returns physically impossible, negative drug concentration estimates near the time that we expect the in vivo drug concentration to instead be reaching its maximum value (Figure 4C). The inability of the Gaussian fit to capture shouldering also causes it to increase, rather than decrease the noise seen in the concentration estimates in our test-bed in vivo data set. To evaluate this quantitatively we employ the assumption that physiology-driven changes in drug concentration should not vary significantly at time scales shorter than ~8 min, which, in the frequency space, corresponds to frequencies above 2 mHz. Consequently, any component of the time-series that falls above this frequency likely arises from measurement noise, rather than from authentic, physiological

https://doi.org/10.1021/acssensors.5c00760
ACS Sens. XXXX, XXX, XXX−XXX

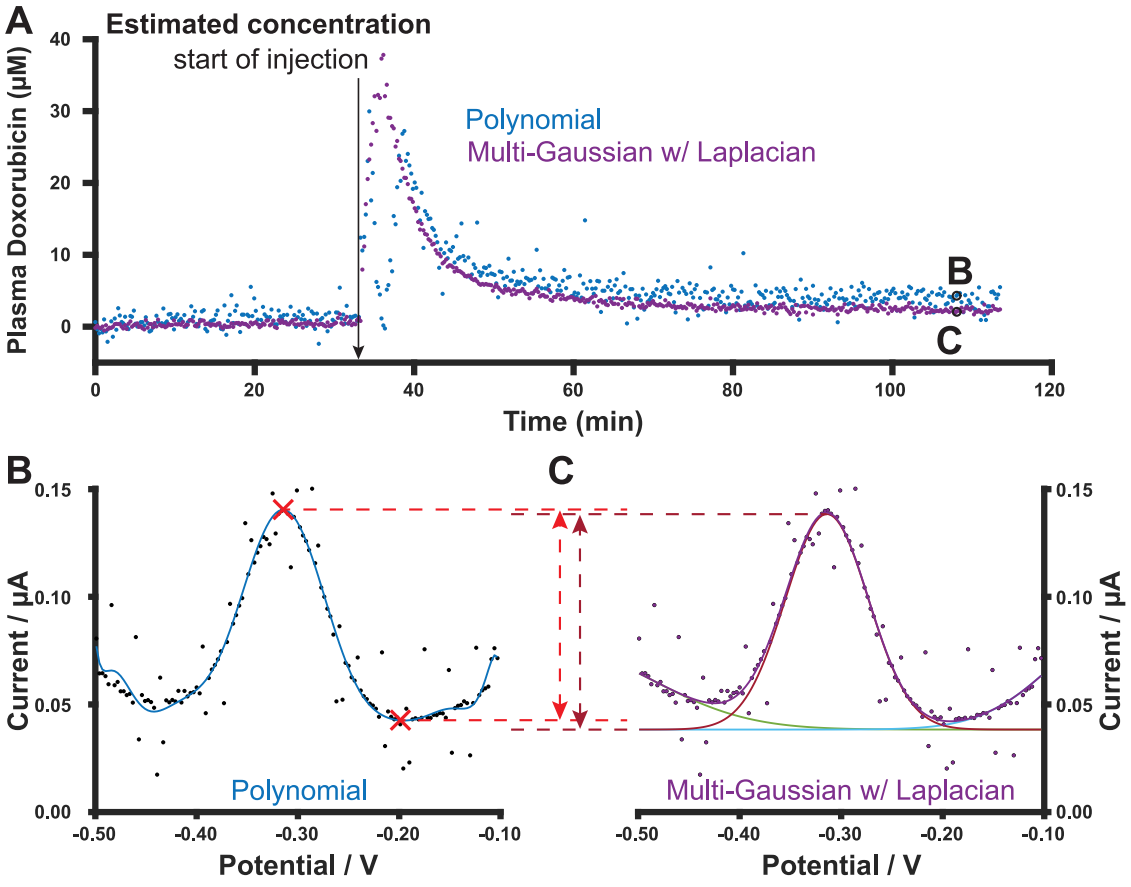

Figure 6. (A) As expected, polynomial and the multi-Gaussian with Laplacian both return mean concentration estimates within error of zero prior to injection of the target analyte. The root-mean-squared noise seen during this period, however, is ∼3-fold lower for the letter fitting approach. In contrast, near the end of this measurement run there is a small, but systematic variation between the concentration estimates provided by the two approaches, with the multi-Gaussian with Laplacian returning slightly lower concentration estimates. (B, C) Inspection of voltammograms at this point in the data collection suggest that this discrepancy is due to shouldering on the right-hand side of the voltammograms that is unaccounted for in the polynomial fit, causing that approach to overestimate the true peak height.

processes. To quantify this high frequency noise, we perform a Fourier transform on the time-series. We then calculate the "fraction" of the total variance that occurs above each given frequency (see Supporting Information (SI) for the precise mathematical formula). At frequencies >2 mHz, the value of this ratio reflects noise. By this metric, we find that our single-Gaussian fit produces more, rather than less noise than the polynomial fit (Figure 4D).

To correct the shouldering problem that degrades both polynomial and single-Gaussian fits, we next introduced two additional Gaussians to our single-Gaussian fit, bringing the total number of Gaussians to 3. We did so under the argument that, like the peak itself, the shoulders also arise due to faradaic processes, such as target oxidation (which dominates in our test bed data set) or oxygen reduction (which can become problematic as the monolayer degrades).[25,26] To ensure accurate and rapid convergence of these "multi-Gaussian" fits we implemented two constraints to the additional Gaussians. First, we constrained them such their centers lay outside of the potential window being scanned, as they are shoulders and not peaks. Second, we constrained their potential widths to ensure that the tails they produce change the estimated height of the redox reporter's peak by less than 5%. The latter, admittedly, is a somewhat arbitrarily selected cutoff, but empirically we find that it works well, leading to rapid and accurate convergence of the fit. For example, although the addition of two more Gaussians increases the number of estimated parameters in our fits to 10, it nevertheless avoids the edge effects that, for the polynomial fit, arise due to overfitting of the animal's pulse (Figure 4A). The multi-Gaussian also accurately corrects the effects of the shouldering on our estimation of peak height (Figure 4B), leading to physiologically (and physically!) meaningful plasma drug concentration estimates near C_{max} in our particularly problematic in vivo data set (Figure 4C). And the multi-Gaussian fit achieves these benefits while also reducing noise relative to both the polynomial and single-Gaussian fits (Figure 4D).

The multi-Gaussian fits accurately capture the peak height of most of our voltammograms, removing the physically or physiologically improbably double-peak in the concentration time course produced by the polynomial and single-Gaussian fits (Figure 4C) Relative to the polynomial fit, however, the reduction in noise seen with the multi-Gaussian approach is fairly modest (Figure 4D). Inspecting the fits to the individual voltammograms, we find that this occurs because the sparse-but-large-and-regular outlier values on the voltammograms produced by the animal's pulse sometimes cause multi-Gaussian fits to incorrectly estimate the voltammogram baseline (Figure 5A).

To solve this, we next implemented L1 norm regularization,[27] an approach that captures these outliers and removes their effect on the baseline estimation. It does so by adding a measurement

https://doi.org/10.1021/acssensors.5c00760
ACS Sens. XXXX, XXX, XXX−XXX

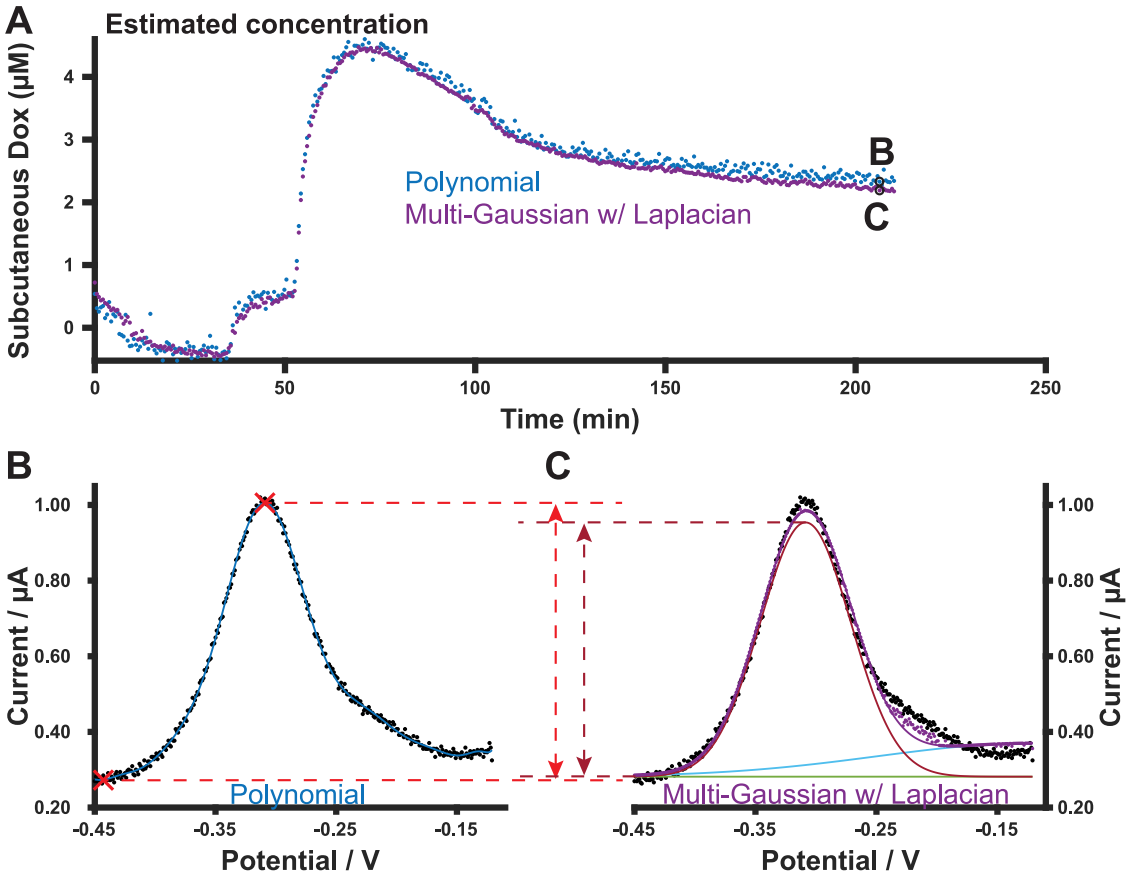

Figure 7. Multi-Gaussian with Laplacian approach works well when applied to sensors placed in other bodily compartments. Shown, for example, are EAB measurements of doxorubicin in the subcutaneous space (interstitial fluid), Data adapted with permission from[21] Copyright 2025, American Chemical Society. The noise produced by the multi-Gaussian w/Laplacian fit is notably less than that produced by the polynomial fit (see Figure SI1).

noise with a Laplacian distribution to the model[28] (for details, see methods). Relative to Gaussian, Laplacian noise has a heavier tail which allows it to better capture the non-Gaussian noise that the animal's pulse produces in our voltammograms (Figure 5B). The resulting improvement in our ability to remove such noise reduces the noise in the in vivo concentration estimates quite significantly (Figure 5C,D).

Multi-Gaussian with Laplacian fitting achieves it improved noise without any concomitant change in accuracy. To see this, we focus on the preinjection baseline in our test-bed data set, a period when the concentration of the drug target is known to be zero (Figure 6A, left-hand side). Consistent with the known zero value of the concentration, mean values produced by the polynomial fit and the multi-Gaussian with Laplacian fit over this period are >0.025 μM, suggesting both are reasonably accurate. In contrast, however, the root-mean-squared values seen during this period are 1.13 and 0.35 μM for the polynomial and multi-Gaussian with Laplacian fits, respectively, illustrating the ∼3-fold reduced noise associated with the latter. This said, at the end of the measurement run the two approaches produce small, but systematically different concentrations estimates (Figure 6A, right-hand side). Inspection of voltammograms collected at this time suggest that this is arising due to shouldering that is not captured by the polynomial fit (Figure 6B) but is captured by the multi-Gaussian with Laplacian fit (Figure 6C).

While we employed only a single, notably problematic plasma doxorubicin data set collected in the jugular vein in the above analysis, the multi-Gaussian with Laplacian approach also reduces the noise in a wide range of other in vivo measurement applications. This includes notably problematic data sets collected from sensors placed in other bodily compartments (Figure 7), and sensors directed against other targets (Figure 8). In every case, the multi-Gaussian with Laplacian reduced high-frequency noise significantly relative to our prior, polynomial fitting approach. And when the average drug concentration estimates produced by the two vary, inspection of the component voltammograms suggests in every case that the discrepancies are arising due to systematic peak-height estimation errors inherent in the polynomial fit.

CONCLUSIONS

There are a number of challenges associated with the use of EAB sensors as a means of performing in vivo drug and metabolite measurements. In the rat jugular vein, for example, which has been a commonly employed measurement site, noise from the animal's pulse introduces significant voltammogram noise, rendering it difficult to accurately estimate concentrations. Similarly, the measurement of electroactive species or the degradation of the sensor's protective monolayer can lead to the introduction of additional Faradaic processes, causing peak shouldering that can be difficult to correct using prior voltammogram fitting approaches. Here, however, we show that multi-Gaussian with Laplacian fitting significantly reduces the noise associated with EAB-derived, in vivo drug concentration measurements. Specifically, by addressing limitations in our previous polynomial fitting approach, particularly in handling noise from physiological sources and addressing peak shouldering, this new fitting method offers a more reliable means

https://doi.org/10.1021/acssensors.5c00760
ACS Sens. XXXX, XXX, XXX−XXX

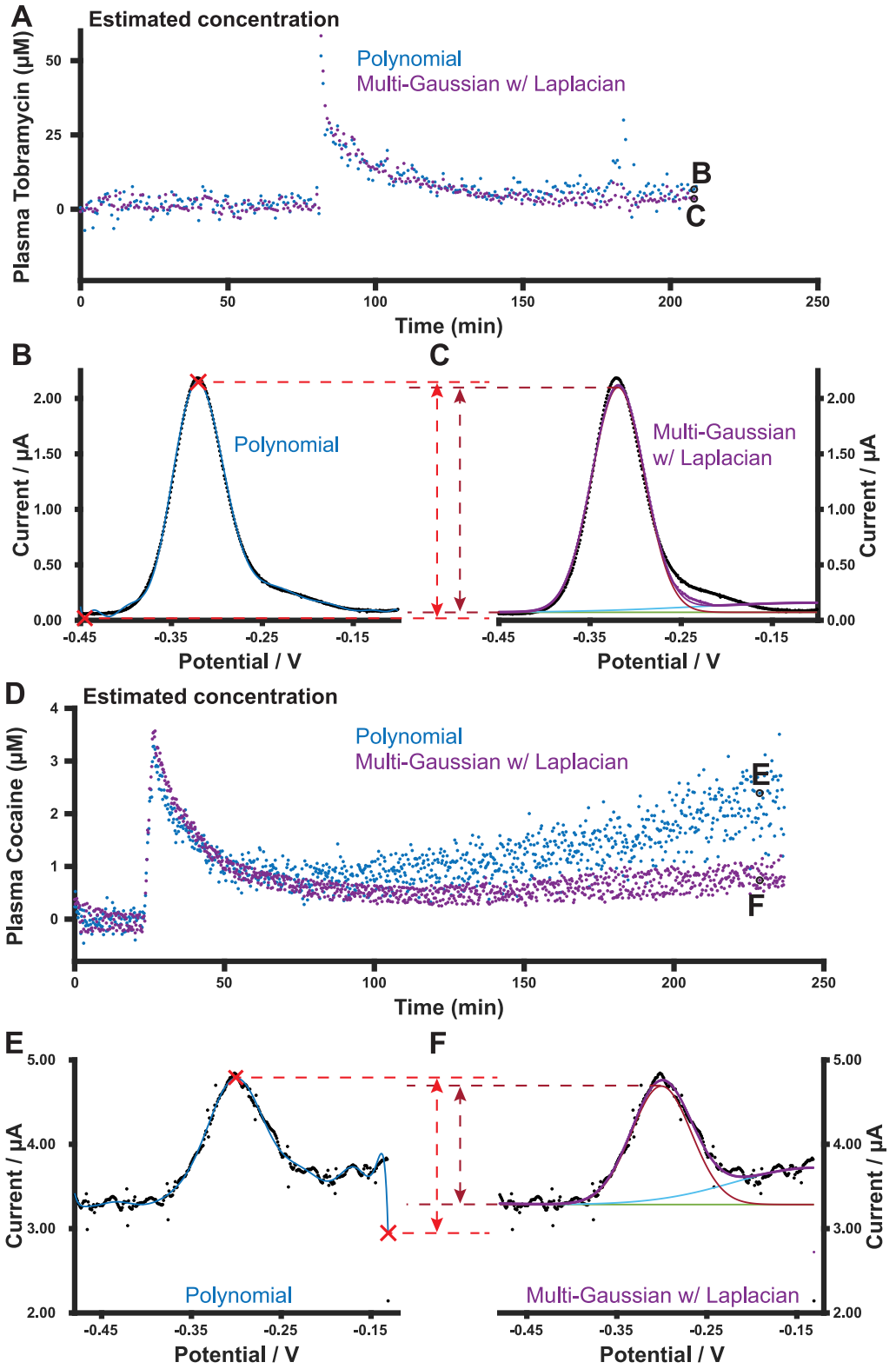

Figure 8. Multi-Gaussian with Laplacian approach works well when applied to sensors against other targets. Shown here are measurements of (A–C) the antibiotic tobramycin and (D–F) the drug of abuse cocaine collected in the rat jugular. Data adapted with permission from[29] Copyright 2024, Wiley-VCH GmbH, and[30] Copyright 2025, American Chemical Society. In both examples, the noise produced by the multi-Gaussian w/Laplacian fit is notably less than that produced by the polynomial fit (see Figure SI1).

of estimating peak heights from the square wave voltammograms most commonly employed in EAB sensor interrogation. Given the potential importance of real-time, minimally invasive monitoring in advancing personalized medicine, these improvements suggest that EAB sensors could serve as a transformative tool for continuous molecular health assessment and therapeutic drug monitoring.

https://doi.org/10.1021/acssensors.5c00760
ACS Sens. XXXX, XXX, XXX−XXX

Table 1. Parameter Constraints and Descriptions

parameter	constraints	description
L [μA]	$L_0 - 0.05\ \mu A < L < L_0 + 0.05\ \mu A$	baseline current, the user defines the upper and lower bounds by specifying the midpoint, L_0
μ_1 [V]	$\mu_c - 0.05\ V < \mu_1 < \mu_c + 0.05\ V$	peak potential of the middle Gaussian, the range is defined by the user-specified midpoint, μ_c
μ_2 [V]	$V_{min} - 0.0913\ V < \mu_2 < V_{min}$	peak potential of the left-hand Gaussian, here V_{min} corresponds to the lower end of the potential range
μ_3 [V]	$V_{max} < \mu_3 < V_{max} + 0.0913\ V$	peak potential of the right-hand Gaussian, here V_{max} corresponds to the upper end of the potential range
c_1 [μA]	$0 < c_1 < c_{1max}$	peak height of the middle Gaussian, with a user specified maximum value, c_{1max}
c_2 [μA]	$0 < c_2 < 2c_{1max}$	peak height of the left-hand Gaussian
c_3 [μA]	$0 < c_3 < 2c_{1max}$	peak height of the right-hand Gaussian
λ_1 [$1/V^2$]	$50 < \lambda_1 < 600$	$\lambda_1 = 1/2\sigma_1^2$ where σ_1 is the standard deviation of the middle Gaussian
λ_2[$1/V^2$]	$30 < \lambda_2 < 100$	$\lambda_2 = 1/2\sigma_2^2$ where σ_2 is the standard deviation of the left-hand Gaussian
λ_3 [$1/V^2$]	$30 < \lambda_3 < 100$	$1/2\sigma_3^2$ where σ_3 is the standard deviation of the right-hand Gaussian
I [μA]	$-1 < I_i < 1$	Laplacian noise term

METHODS

In our efforts we employ a Gaussian function of form

$$\underline{y} = L + c\,e^{-\lambda(x-\mu)^2} \tag{1}$$

where L is the baseline current of the voltammogram, c is the peak current, λ is a measure of the width of the voltammogram and μ is potential at which the peak is located. We also assume the Gaussian is "contaminated" with independent, zero-mean Gaussian noise with a distribution $n_i \sim N(0,\sigma^2)$. Given this, our measurements become

$$\boldsymbol{y} = L + c\,e^{-\lambda(\boldsymbol{x}-\mu)^2} + \boldsymbol{n} \tag{2}$$

To compute the parameters of this function based on our observed voltammograms, we employed maximum likelihood estimation, which finds the parameters that maximizes the likelihood function

$$\prod_{i=1}^{m} \frac{1}{\sqrt{2\pi}\sigma} e^{-(y_i-\overline{y}_i)^2/2\sigma^2} \tag{3}$$

To simplify our calculations, we take the negative log-likelihood, such that our optimization problem becomes

$$\underset{L,c,\lambda,\mu}{\operatorname{argmin}} \sum_{i=1}^{m} (y_i - \overline{y}_i)^2 \tag{4}$$

This optimization can be solved numerically using the algorithm discussed shortly.

To perform multi-Gaussian fits, we simply changed our fitted curve to the sum of 3 Gaussians and applied the same procedure as above.

$$\boldsymbol{y} = L + c_1 e^{-\lambda_1(\boldsymbol{x}-\mu_1)^2} + c_2 e^{-\lambda_2(\boldsymbol{x}-\mu_2)^2} + c_3 e^{-\lambda_3(\boldsymbol{x}-\mu_3)^2} + \boldsymbol{n} \tag{5}$$

Finally, to capture the outlier points using L1 normalization, we added an additional noise term, I, to eq 5 that we assume has zero-mean Laplace distribution $\left(\frac{1}{2b}e^{-|x|/b}\right)$ and independent from the zero-mean Gaussian noise. We thus fit our measurements to

$$\boldsymbol{y} = L + c_1 e^{-\lambda_1(\boldsymbol{x}-\mu_1)^2} + c_2 e^{-\lambda_2(\boldsymbol{x}-\mu_2)^2} + c_3 e^{-\lambda_3(\boldsymbol{x}-\mu_3)^2} + \boldsymbol{n} + \boldsymbol{I} \tag{6}$$

With the addition of the I term, the likelihood function of the maximum likelihood estimation becomes

$$\prod_{i=1}^{m} \frac{1}{\sqrt{2\pi}\sigma} \frac{1}{2b} e^{-(y_i-\overline{y}_i-I_i)^2/2\sigma^2} e^{-|I_i|/b} \tag{7}$$

Then, since logarithm is a monotonic function, we take the symmetric of the logarithm of the likelihood and we minimize the resulting expression below

$$\underset{L,c,\lambda,\mu,I,\overline{\sigma},\overline{b}}{\operatorname{argmin}} \frac{1}{2}\left(\frac{\overline{\sigma}}{m}\|\boldsymbol{y}-\overline{\boldsymbol{y}}-\boldsymbol{I}\|_2^2 - \log\overline{\sigma}\right) + \left(\frac{\overline{b}}{m}\|\boldsymbol{I}\|_1 - \log\overline{b}\right) \tag{8}$$

where $\overline{\sigma} = \frac{1}{\sigma^2}$, $\overline{b} = \frac{1}{b}$.

All optimization problems above were solved using IPOPT solver[31] in CasADi,[32] an open-source tool for nonlinear optimization, using MATLAB.

To ensure that our optimization converges rapidly, we added constraints to the optimization above. First, since we observe only a single peak within the potential window, we force the peak positions of the other two Gaussians (μ_2 and μ_3) to be outside of the window, one at lower potentials and the other at higher potentials. Second, we constrain the magnitude of the two additional Gaussians such that they contribute less than 5% to the peak current of the middle Gaussian. The latter is a rather arbitrary constraint, but empirically we have found that it works well. In addition to these constraints, we also employ parameter bounds (Table 1), which are either user defined or are fixed at values that produce good results for all of the data sets we have considered. In the future, we will update the values of these bounds in the code if we encounter new data sets that require us to fine-tune them. Note that, instead of solving eq 8, our numerical implementation of this algorithm solves a close approximation of that can be solved much more efficiently. For details, see the Supporting Information.

ASSOCIATED CONTENT

Supporting Information

The Supporting Information is available free of charge at https://pubs.acs.org/doi/10.1021/acssensors.5c00760.

Solution to the minimization in eq 8 and the fraction of the total variance analysis of the data sets in (Figures 8 and 9) (PDF)

Primer describing the operation of the relevant software (PDF)

AUTHOR INFORMATION

Corresponding Author

Kevin W. Plaxco − *Department of Chemistry and Biochemistry, University of California, Santa Barbara, California 93106, United States; BioEngineering Department, University of California Santa Barbara, Santa Barbara, California 93106, United States;* orcid.org/0000-0003-4772-8771; Email: kwp@ucsb.edu

Authors

Zeki Duman − *Department of Electrical and Computer Engineering, University of California, Santa Barbara, California 93106, United States;* orcid.org/0009-0007-1824-2007

Nicole A. Emmons − *Department of Psychological and Brain Sciences, University of California, Santa Barbara, California 93106, United States;* orcid.org/0000-0002-5275-2613

https://doi.org/10.1021/acssensors.5c00760
ACS Sens. XXXX, XXX, XXX−XXX

Tod E. Kippin − *Department of Psychological and Brain Sciences, University of California, Santa Barbara, California 93106, United States*
Lior Sepunaru − *Department of Chemistry and Biochemistry, University of California, Santa Barbara, California 93106, United States;* orcid.org/0000-0002-4716-5035
João Hespanha − *Department of Electrical and Computer Engineering, University of California, Santa Barbara, California 93106, United States;* orcid.org/0000-0003-2809-4718

Complete contact information is available at: https://pubs.acs.org/10.1021/acssensors.5c00760

Notes

The authors declare the following competing financial interest(s): KWP is a consultant for and owns equity in a company commercializing electrochemical aptamer-based sensors. NAE is employed by a company commercializing aptamer-based sensors.

■ ACKNOWLEDGMENTS

The authors wish to thank our many co-workers and colleagues who advised us regarding the scope of the problem and helped to test-run the code and the primer. This work was supported by the National Institutes of Health grant EB022015.

■ REFERENCES

(1) Arroyo-Currás, N.; Ortega, G.; Copp, D. A.; Ploense, K. L.; Plaxco, Z. A.; Kippin, T. E.; Hespanha, J. P.; Plaxco, K. W. High-precision control of plasma drug levels using feedback-controlled dosing. *ACS Pharmacol. Transl. Sci.* **2018**, *1*, 110−118.
(2) Gerson, J.; Erdal, M. K.; McDonough, M. H.; Ploense, K. L.; Dauphin-Ducharme, P.; Honeywell, K.; Leung, K.; Arroyo-Curras, N.; Gibson, J.; Emmons, N. A.; Meiring, W.; Meiring, W.; Hespanha, J.; Hespanha, J. P.; Plaxco, K. W.; Plaxco, K. W.; Kippin, T. High-precision monitoring of and feedback control over drug concentrations in the brains of freely-moving rats. *Sci. Adv.* **2023**, *9*, No. eadg3254.
(3) Arroyo-Curras, N.; Somerson, J.; Vieira, P.; Ploense, K.; Kippin, T.; Plaxco, K. W. Real-time measurement of small molecules in awake, ambulatory animals. *Proc. Natl. Acad. Sci. U.S.A.* **2017**, *114*, 645−650.
(4) Idili, A.; Arroyo-Currás, N.; Ploense, K. L.; Csordas, A. T.; Kuwahara, M.; Kippin, T. E.; Plaxco, K. W. Seconds-resolved pharmacokinetic measurements of the chemotherapeutic irinotecan in situ in the living body. *Chem. Sci.* **2019**, *10*, 8164−8170.
(5) Dauphin-Ducharme, P.; Yang, K.; Arroyo-Currás, N.; Ploense, K. L.; Zhang, Y.; Gerson, J.; Kurnik, M.; Kippin, T. E.; Stojanovic, M. N.; Plaxco, K. W. Electrochemical aptamer-based sensors for improved therapeutic drug monitoring and high-precision, feedback-controlled drug delivery. *ACS Sens.* **2019**, *4*, 2832−2837.
(6) Idili, A.; Gerson, J.; Kippin, T.; Plaxco, K. W. Seconds-resolved, in situ measurements of plasma phenylalanine disposition kinetics in living rats. *Anal. Chem.* **2021**, *93*, 4023−4032.
(7) Chamorro-Garcia, A.; Gerson, J.; Flatebo, C.; Fetter, L.; Downs, A. M.; Emmons, N.; Ennis, H. L.; Milosavić, N.; Yang, K.; Stojanovic, M.; Ricci, F.; Kippin, T. E.; Plaxco, K. W. Real-time, seconds-resolved measurements of plasma methotrexate in Situ in the living body. *ACS Sens.* **2023**, *8*, 150−157.
(8) Seo, J.-W.; Fu, K.; Correa, S.; Eisenstein, M.; Appel, E. A.; Soh, H. T. Real-time monitoring of drug pharmacokinetics within tumor tissue in live animals. *Sci. Adv.* **2022**, *8*, No. eabk2901.
(9) Lin, S.; Cheng, X.; Zhu, J.; Wang, B.; Jelinek, D.; Zhao, Y.; Wu, T.; Horrillo, A.; Tan, J.; Yeung, J.; Yan, W.; Forman, S.; Coller, H. A.; Milla, C.; Emaminejad, S. Wearable microneedle-based electrochemical aptamer biosensing for precision dosing of drugs with narrow therapeutic windows. *Sci. Adv.* **2022**, *8*, No. eabq4539.
(10) Shaver, A.; Mahlum, J. D.; Scida, K.; Johnston, M. L.; Pellitero, M. A.; Wu, Y.; Carr, G. V.; Arroyo-Currás, N. Optimization of vancomycin aptamer sequence length increases the sensitivity of electrochemical aptamer-Based sensors in vivo. *ACS Sens.* **2022**, *7*, 3895−3905.
(11) Nguyen, M. D.; Nguyen, K. N.; Malo, S.; Banerjee, I.; Wu, D.; Du-Thumm, L.; Dauphin-Ducharme, P. Electrochemical aptamer-based biosensors for measurements in undiluted human saliva. *ACS Sens.* **2023**, *8*, 4625−4635.
(12) Bakhshandeh, F.; Zheng, H.; Barra, N. G.; Sadeghzadeh, S.; Sadgehzadeh, I. A.; Ausri, I.; Sen, P.; Sen, P.; Keyvani, F.; Keyvani, F.; Rahman, F.; Rahman, F.; Quadrilatero, J.; Quadrilatero, J.; Liu, J.; Liu, J.; Schertzer, J. D.; Schertzer, J. D.; Soleymani, L.; Soleymani, L.; Poudineh, M. Wearable aptalyzer integrates microneedle and electrochemical sensing for in vivo monitoring of glucose and lactate in live animals. *Adv. Mater.* **2024**, *36*, No. e2313743.
(13) Dauphin-Ducharme, P.; Arroyo-Curras, N.; Adhikari, R.; Somerson, J.; Ortega, G.; Makarov, D. E.; Plaxco, K. W. Chain dynamics limit electron transfer from electrode-bound, single-stranded oligonucleotides. *J. Phys. Chem. C* **2018**, *122*, 21441−21448.
(14) Gerson, J.; Erdal, M. K.; Dauphin-Ducharme, P.; Emmons, N.; Idili, A.; Hespanha, J.; Hespanha, J. P.; Plaxco, K. W.; Plaxco, K. W.; Kippin, T. E. A high-precision view of intercompartmental drug transport via simultaneous, seconds-resolved, in situ measurements in the vein and brain. *Br. J. Pharmacol.* **2024**, *181*, No. eadg3254.
(15) Soleimani, S.; Arkan, E.; Jalalvand, A. R.; Goicoechea, H. C. Fabrication of a novel electrochemical aptasensor assisted by a novel computerized monitoring system for real-time determination of the prostate specific antigen: A computerized experimental method brought elegancy. *Microchem. J.* **2020**, *157*, No. 104898.
(16) Idili, A.; Bonini, A.; Parolo, C.; Alvarez-Diduk, R.; Di Francesco, F.; Merkoçi, A. A programmable electrochemical Y-shaped DNA scaffold sensor for the single-step detection of antibodies and proteins in untreated biological fluids. *Adv. Funct. Mater.* **2022**, *32*, No. 2201881.
(17) Abeykoon, S. W.; White, R. J. Single voltammetric sweep calibration-free interrogation of electrochemical aptamer-based sensors employing continuous square wave voltammetry. *Anal. Chem.* **2024**, *96*, 6958−6967.
(18) Savitzky, A.; Golay, M. J. E. Smoothing and differentiation of data by Simplified Least Squares Procedures. *Anal. Chem.* **1964**, *36*, 1627−1639.
(19) Schmid, M.; Rath, D.; Diebold, U. Why and how Savitzky−Golay filters should be replaced. *ACS Meas. Sci. Au* **2022**, *2*, 185−196.
(20) Curtis, S. D.; Ploense, K. L.; Kurnik, M.; Ortega, G.; Parolo, C.; Kippin, T. E.; Plaxco, K. W.; Arroyo-Currás, N. Open source software for the real-time control, processing, and visualization of high-volume electrochemical data. *Anal. Chem.* **2019**, *91*, 12321−12326.
(21) Emmons, N. A.; Gibson, J. M.; McDonough, M. H.; Gerson, J.; Erdal, M.; Leung, K. K.; Fetter, L. C.; Plaxco, K. W.; Plaxco, K. W.; Kippin, T. E. Simultaneous, seconds-resolved doxorubicin measurements in the blood and subcutaneous interstitial fluid identify quantitative pharmacokinetic relationships between the two. *ACS Pharm. Trans. Sci.* **2025**, *8* (5), 1347−1358, DOI: 10.1021/acsptsci.5c00062.
(22) Leung, K. K.; Gerson, J.; Emmons, N.; Roehrich, B.; Verrinder, E.; Fetter, L.; Fetter, L. C.; Kippin, T.; Kippin, T. E.; Plaxco, K. W. A tight squeeze: geometric effects on the performance of three-electrode electrochemical-aptamer based sensors in constrained, in-vivo placements. *Analyst* **2023**, *148*, 1562−1569.
(23) Yi, C.; Gratzl, M. Continuous in situ electrochemical monitoring of doxorubicin efflux from sensitive and drug-resistant cancer cells. *Biophys. J.* **1998**, *75*, 2255−2261.
(24) Gulaboski, R.; Mirceski, V. Calculating of square-wave voltammograms—a practical on-line simulation platform. *J. Solid State Chem.* **2024**, *28*, 1121−1130.
(25) Leung, K. K.; Downs, A. M.; Ortega, G.; Kurnik, M.; Plaxco, K. W. Elucidating the mechanisms underlying the signal drift of electrochemical aptamer-based sensors in whole blood. *ACS Sens.* **2021**, *6*, 3340−3347.

(26) Downs, A. M.; Plaxco, K. W. Real-time, in vivo molecular monitoring using electrochemical aptamer-based sensors: opportunities and challenges. *ACS Sens.* **2022**, *7*, 2823−2832.
(27) Ke, Q.; Kanade, T. *Robust l/Sub 1/Norm Factorization in the Presence of Outliers and Missing Data by Alternative Convex Programming*, IEEE Comput. Soc. Conf. Comput. Vis. Pattern Recognit; IEEE, 2005; pp 739−746.
(28) Carrillo, L. R. G.; Russell, W. J.; Hespanha, J. P.; Collins, G. E. State estimation of multiagent systems under impulsive noise and disturbances. *IEEE Trans. Control Syst. Technol.* **2015**, *23* (1), 13−26.
(29) Leung, K. K.; Gerson, J.; Emmons, N.; Heemstra, J. M.; Kippin, T. E.; Plaxco, K. W. The use of xenonucleic acids significantly reduces the in vivo drift of electrochemical aptamer-based sensors. *Angew. Chem., Int. Ed.* **2024**, *63*, No. e202316678.
(30) Alkhamis, O.; Canoura, J.; Wu, Y.; Emmons, N.; Wang, Y.; Honeywell, K. M.; Plaxco, K. W.; Kippin, T. E.; Xiao, Y. High-affinity aptamers for in vitro and in vivo cocaine sensing. *J. Am. Chem. Soc.* **2024**, *146*, 3230−3240.
(31) Wächter, A.; Biegler, L. T. On the implementation of a primal-dual interior point filter line search algorithm for large-scale nonlinear programming. *Math. Program.* **2006**, *106*, 25−57.
(32) Andersson, J. A. E.; Gillis, J.; Horn, G.; et al. CasADi: a software framework for nonlinear optimization and optimal control. *Math. Program. Comput.* **2019**, *11*, 1−36.
(33) Mistry, A.; Franco, A. A.; Cooper, S. J.; Robets, S. A.; Viswanathan, V. How machine learning will revolutionize electrochemical sciences. *ACS Energy Lett.* **2021**, *6*, 1422−1431.
(34) Adams, A. C.; Jha, S.; Lary, D. J.; Slinker, J. D. Machine learning for estimating electron transfer rates from square wave voltammetry. *ChemPlusChem* **2022**, *87*, No. e202100418.
(35) Cobb, S. J.; Macpherson, J. V. Enhancing square wave voltammetry measurements via electrochemical analysis of the non-faradaic potential window. *Anal. Chem.* **2019**, *91*, 7935−7942.

https://doi.org/10.1021/acssensors.5c00760
ACS Sens. XXXX, XXX, XXX−XXX